Minimizing deformation of a thin fluid film driven by fluxes of momentum and heat

Davin Lunz*
Inria Saclay – Île de France, 91120 Palaiseau, France;
École Polytechnique, CMAP 91128 Palaiseau, France;
Institut Pasteur, 75015 Paris, France;
and University of Oxford, Mathematical Institute, Andrew Wiles Building, Oxford OX2 6GG, United Kingdom

(Received 8 November 2020; accepted 24 February 2021; published 16 March 2021)

We consider a thin fluid film flowing down an inclined substrate subjected to localized external sources of momentum and heat flux that induce deformations of the fluid's free surface. This scenario is encountered in several industrial processes and of particular interest is the case where these deformations are undesirable. When the substrate is thin and the temperature along its underside is freely imposed by an active cooling mechanism, temperature gradients are generated at the fluid surface which drive a thermocapillary flow and influence the deformations. This naturally leads us to pose the optimal control problem of choosing the temperature profile that minimizes the unwanted free-surface deformations. Numerical computations reveal that the external forces generate deflections in a region near their peak beyond which all deflections are suppressed by the optimal control. Where nonzero deflections occur, the control is of bang-bang type (taking either its upper or lower bound), while the control is obtained in closed form for regions where the deflections are suppressed. Strikingly, in switching between these regions the optimal control chatters, that is, it switches infinitely many times over a finite interval. By appealing to Pontryagin's maximum principle and leveraging a symmetry embedded in the adjoint problem we uncover the underlying fractal structure of the chattering. Finally, we present practical approaches to avoid the infinite switching while retaining significantly reduced free-surface deformations.

DOI: 10.1103/PhysRevE.103.033105

I. INTRODUCTION

Thin fluid films are ubiquitous in both industrial and biological settings [1–3]. The prevalence of thin fluid films stems from the rich set of behaviors they exhibit, which endows them with a unique versatility and manipulability. In many applications the fluid film is subjected to an external, spatially varying pressure or heat load, which causes the surface to deviate from a flat profile by inducing a spatially inhomogeneous flow. For example, in nuclear fusion research, which aims at providing clean, safe, and fuel-abundant baseload power, one technological roadblock is dealing with the heat load that escapes the core confinement region and must be exhausted within the vessel without causing excessive damage. A thin liquid metal film covering a solid substrate is one promising direction that may be capable of sustaining the predicted load [[4–6], and references within]. Other industrial applications are described by flow of a thin film along a substrate subjected to an external pressure load, including material processing such as jet-stripping and blade coating [[7–10], and references within], microfluidics applications [11], biomedical engineering, as well as in the food and chemical industries [12]. This catalog of applications motivates the present study, in which we consider the flow of a thin incompressible, viscous fluid down a thin inclined plane, driven by gravity and an external jet of momentum and heat flux.

While in some instances it might be advantageous to induce free-surface deformations (for example, to enhance heat transfer [13–15]), in this paper we are concerned with the case when these deformations are unwanted. For example, in the nuclear fusion context, deformations can make the fluid susceptible to dangerous ejection and dry-out events. In blade coating, the aim is to avoid deformations to produce a uniform coating. It is thus desirable to attempt to design relevant system parameters to minimize deflections by, for example, tuning the forcing magnitudes, carefully selecting material properties, or customising the system geometry. Inspired by the fusion context where the thermal load is significant, we consider active substrate cooling where we may choose a temperature profile to be imposed on the underside of the substrate along which the fluid flows. The applied cooling induces thermal gradients at the fluid surface, which drive a thermocapillary flow and ultimately influence the free-surface deflections. This naturally leads us to pose the optimal control problem of selecting the cooling profile that minimizes the free-surface deflections.

Two formulations for control problems appear in the literature: closed-loop control (also called feedback control) describes where the state of the system is used as the control input, while open-loop control is independent of system feedback but may depend on other independent variables (such as time). Optimal control seeks to determine a control law that optimizes some functional of the system dynamics and may be posed in an open-loop or closed-loop formulation (see [[16], Sec. 2.2] or [[17], Sec. 5.2]). An open-loop optimal control may steer the system dynamics along an unstable trajectory or might exhibit sensitivity due to model or actuator error [18]. It is thus typical to incorporate a feedback loop to stabilize the optimal trajectory, ensuring the optimal control is realized

*davin.lunz@inria.fr

 ©2021 American Physical Society

robustly. In this way, open-loop optimal control and feedback control can complement each other: feedback control can be employed to robustly steer the system along an ideal system trajectory determined by the open-loop optimal control problem.

Precise control of fluid flow is necessary in several industrial and biological applications and has thus received much attention in the literature. Feedback control of fluid systems has been shown to stabilize contact line instabilities [19], evaporatively driven instabilities [20], as well as suppress Marangoni-Bénard [21] and Rayleigh-Bénard convection [22]. All of these studies employ thermal effects to influence the fluid dynamics. In addition to thermal influences, nonuniform substrate topography [23], electromagnetic fields [24–28], external air blowing and suction [29], and fluid injection and extraction [30] have been explored as a source of influence on the fluid interface. Feedback control using fluid injection and extraction [31–33] has been employed to suppress waves in weakly nonlinear models of thin films and to optimize actuator placement. The case of open-loop optimal control via fluid injection and extraction has also been recently considered [34].

In this paper we focus on the open-loop optimal control problem of minimizing the steady-state free-surface deflections by steady, spatially inhomogeneous substrate cooling. We emphasize that the independent variable of the system and control is typically time; however, in this steady formulation the independent variable is space. Thus, to reiterate, we aim to design the spatially inhomogeneous cooling profile so as to minimize the film deformation. While we demonstrate that studying the two-dimensional steady-state problem is justified, this does not exclude three-dimensional instabilities, which are not considered in this work.

Since the Bond number—representing the ratio of gravitational forces to capillary forces due to surface curvature—is typically large (see Appendix A), it might be tempting to neglect the capillary forces in a leading-order model. However, the importance of surface tension in the normal interfacial stress condition, as first elucidated by Benney [35] and Gjevik [36], plays an important role in thin-film flow [2], especially in the presence of small-scale disturbances, such as narrow jets impinging upon the fluid as present in this study. With this in mind we present results for both cases: first neglecting stresses due to surface tension in the normal direction of the fluid interface and subsequently reinstating it. We henceforth refer to the normal surface tension stress as "normal capillarity" to distinguish it from the tangentially oriented Marangoni stresses, which we refer to as thermocapillarity (and retain in all cases, as this is the mechanism by which the control acts). Neglecting the normal capillarity serves as an instructive stepping stone to the full model. The stark difference between the controls for these two cases reinforces the important role surface tension plays in morphological control of thin films. Moreover, the comparison provides analytical insight into the system structure that gives rise to the chattering phenomenon manifest in the full system.

In the first case, where normal capillarity is neglected, we find that the deflections may persist only in the vicinity of the peak forcing. In these regions the optimal control is of bang-bang type, that is, the control takes the value of either its upper or lower bound. Beyond these regions all deflections are suppressed, and the optimal control is obtainable in closed form.

In the second case, when the higher-order, normal capillary terms are reinstated, we find similarly that the solution comprises a region in the vicinity of peak forcing where deflections may persist, beyond which deflections are suppressed. However, the optimal control exhibits chattering at the junctions (the points connecting these regions), whereby the bang-bang control switches infinitely many times between its upper and lower bound over a finite interval. We investigate the chattering analytically using Pontryagin's maximum principle (PMP) and by approximating a function whose zeros coincide with the points at which the bang-bang optimal control switches value. The approximation respects a symmetry that allows us to construct self-similar solutions, and we show that the roots align remarkably well with the computed chattering control.

In an industrial setting, a chattering active cooling strategy is not feasible to implement. This motivates our discussion of approaches that regularize the infinite switching. We highlight one particular method that is simple to implement and exhibits near-optimal performance.

The paper is organized as follows. In Sec. II we introduce the steady thin-film equation to be controlled and formulate the optimal control problem. In Sec. III we study the toy model without normal capillarity, which serves as a simple setting to discuss numerical approaches for the optimal control problem. In Sec. IV we reinstate normal capillarity and analyze the chattering optimal cooling profile. In Sec. V we consider practical techniques to regularize the chattering. Finally, in Sec. VI we summarize our findings.

II. THE STEADY THIN-FILM EQUATION AND PROBLEM STATEMENT

A complete mathematical derivation from the governing equations describing mass, momentum, and energy conservation, including concrete dimensional parameter values and associated scalings, may be found in Appendix A. We distill from this analysis the steady-state formulation of the equation governing the deviation of the fluid's free surface from the undisturbed profile. We consider the two-dimensional geometry illustrated in Fig. 1, where x is the downstream coordinate parallel to the substrate, $T^-(x)$ is the idealized temperature profile imposed at the substrate boundary, and $p(x)$ denotes the known profile of the imposed interfacial pressure and normal heat flux (such as in [37]). The pressure and heat source profile $p(x)$ is stationary (not varying in time), spatially inhomogeneous, localized at the origin, and decays in the far field. It may be useful to think of the single source as a jet imparting a flux of momentum and heat to the fluid. Should one wish, there is no additional complexity in considering the momentum and heat fluxes to have different spatial profiles. However, it is not atypical that a single impinging jet is responsible for the transfer of both heat and momentum. Tangential stresses have been neglected.

We note that the cooling mechanism illustrated in Fig. 1 employs discretely spaced cooling channels. This is merely one potential implementation of active cooling, while other

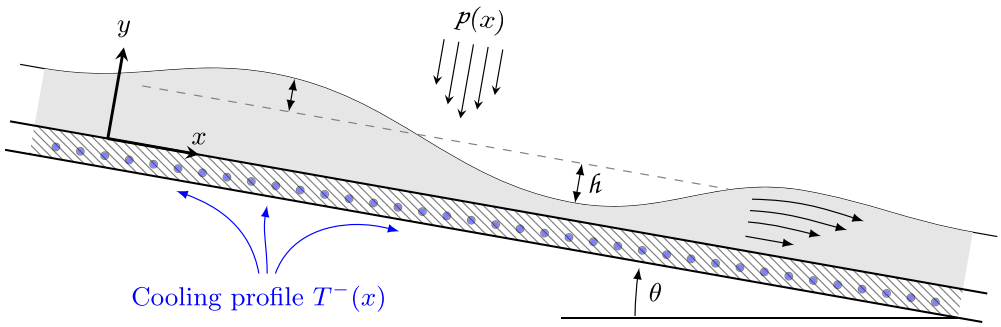

FIG. 1. Schematic of the flow configuration. Circles along the lower side of the substrate indicate cooling channels, which we idealize by imposing an arbitrary temperature profile $T^-(x)$ on the underside of the substrate. The deviations from the undisturbed state (dashed line) are denoted $h(x)$.

implementations, such as coolant jets aimed at the underside of the substrate, may in fact be continuous. We choose to abstract away the precise mechanical implementation details by modeling an idealized substrate temperature profile $T^-(x)$, independent of the underlying mechanism.

Typically, thin-film equations describe the evolution of the film thickness [1–3]. We emphasize that the central quantity in this paper is the free-surface deflection, denoted h, defined as the deviation of the film thickness from its undisturbed fully developed state, that is, in the absence of external forcing and active cooling. Using the lubrication approximation, one may show that this quantity is governed by a thin-film equation of the (dimensionless) form

$$Q(h)\left(1 - A\frac{dp}{dx} - \alpha\frac{dh}{dx} + \beta\frac{d^3h}{dx^3}\right) - B\mathcal{T}(h)\left(\frac{d}{dx}\left[(h+1+\iota)p\right] + \frac{dT^-}{dx}\right) = Q(0), \qquad (1)$$

where Q and $\mathcal{T}$ are the flux functions associated with bulk and thermocapillary forcing, respectively, A is the magnitude of the external pressure forcing, α measures the effect of the transverse component of gravity, β measures the normal capillary forces due to surface tension, B measures the significance of thermocapillary flow, and ι measures the thermal insulation of the substrate. For the sake of completeness, in Appendix A we derive Eq. (1) in the case of hydrodynamic flow, where Q and $\mathcal{T}$ take the forms

$$Q(h) = \frac{(1+h)^3}{3}, \quad \mathcal{T}(h) = \frac{(1+h)^2}{2}, \qquad (2)$$

and the undisturbed film thickness is unity. We highlight that, while we present numerical results exclusively for hydrodynamic flow, the underlying phenomenon persists qualitatively across other flow regimes. For example, the nuclear fusion scenario introduced in Sec. I is characterized by magnetohydrodynamic flow, for which a thin-film equation of form (1) may be derived with flux functions Q and $\mathcal{T}$ encapsulating the magnetohydrodynamic flux [38]. The results in this paper are qualitatively preserved in the magnetohydrodynamic case [5].

We emphasize that only the steady-state formulation of (1) is considered in this work, necessitating a discussion of the stability of the free-surface flow. A more detailed account is given at the end of Appendix A. In brief, as long as the lubrication approximation remains valid, the flow remains noninertial and the Kapitza instability [39,40] will not manifest. Transient nonlinear numerical simulations demonstrate the stability of the two-dimensional problem. A noninertial source of interfacial instability of thin nonisothermal fluid films stems from the interaction between the film morphology, gravity, and thermocapillarity [41,42]. The influence of Marangoni stresses has been shown to result in spanwise modes becoming unstable in some region of parameter space, leading to the formation of rivulets. Despite the physical parameters adopted in this work being in the stable region of parameter space, the problem studied in this work is not identical to those previously investigated, and thus its full three-dimensional stability (or that of a magnetohydrodynamic counterpart) is yet to be established but beyond the scope of this work.

For a general initial film profile, the deviation of the initial conditions from the steady-state profile manifests in a deflection that is advected downstream from the origin as a traveling wave. It might be tempting to think that this invalidates the steady formulation. However, in practice the substrate is of finite length, and such traveling waves are advected through the outlet and out of the system. Thus, in considering the steady state we implicitly consider a sufficiently large time such that we may ignore the unsteady traveling wave that has long since vanished and focus on the fully developed steady-state profile to which the film relaxes.

Given the governing equation (1), we turn our attention to the control aspect of the fluid deflections. The physical quantity directly under our control is the temperature profile $T^-(x)$. From the deflection equation (1), we see that T^- alters the deflections only through its gradient (as only temperature gradients induce thermocapillary flow); therefore we take the temperature gradient to be the control law, denoted $u = dT^-/dx$. In practice, cooling channels (as illustrated in Fig. 1) or impinging cooling jets are spaced at some nonzero distance apart. Typically there will also be constraints on the absolute temperature range in which the system can operate, for example, to avoid evaporation, boiling, and cavitation, as well as material constraints and a limited available cooling power. The bound on absolute temperature differences ΔT of sources separated by some Δx may be expressed as a bound on the admissible temperature gradients, $|u| \leqslant U := \Delta T/\Delta x$.

We now look to formulate a functional that quantifies the deflections $\hbar(x)$. For the sake of simplicity, we begin the analysis by considering the L^2 norm of the deflections

$$\|\hbar\|_2^2 = \int_{-X}^{X} \hbar(x)^2 dx \tag{3}$$

over some finite (but sufficiently large) domain $[-X, X]$. We will subsequently see why there is no loss in generality from considering the infinite domain. In Sec. V we will also discuss more general norms, including terms involving the control u and the derivative of $\hbar$.

With this formulation we pose the optimal control problem, namely,

$$\min_{|u|\leqslant U} \frac{1}{2}\|\hbar(x;u)\|_2^2, \tag{4}$$

where $\hbar$ is subject to the deflection equation (1).

At first glance it may seem that the physical problem (4) is lacking boundary conditions for $\hbar$. However, as an optimization problem the presence of boundary conditions is implicit [43]. To understand this, note that costate variables are introduced in applying the PMP. The lack of boundary conditions on the state results in additional boundary conditions on the costate to produce a system of first-order ordinary differential equations (ODEs) with the same number of boundary conditions as unknown variables, as expected. In this particular problem, this nuance is of little consequence: we will see that sufficiently far from the origin all optimal deflections are completely suppressed. Thus the support of the deflections $\hbar$ will be confined to a region around the origin. It is for this reason that choosing a finite domain $[-X, X]$ sacrifices no generality, and we may choose to set $\hbar$ (and its derivatives) to zero at the boundaries with no change to the results.

At the outset we may determine the unconstrained optimizer. To do so we need a control that ensures the L^2 norm of $\hbar$ is minimal. The obvious candidate for $\hbar$ is the best-case scenario: zero deflections. Substituting $\hbar = 0$ into (1), we can solve for the unconstrained optimal control $u = u_\infty$ to give

$$u_\infty = -\left(\frac{A\mathcal{Q}(0)}{B\mathcal{T}(0)} + 1 + \iota\right)\frac{dp}{dx}. \tag{5}$$

The solution (5) is nothing other than dp/dx scaled by a constant. Physically, u_∞ induces a thermocapillary forcing that precisely balances the deflections driven by the thermocapillarity and pressure induced by the external forcing. We will see that this unconstrained control provides a key ingredient in the constrained optimal control problem.

For the purpose of brevity, we do not explore the effects of varying each of the system parameters or forcing profiles. For an in-depth discussion of these results, we refer the reader to [5,38]. Broadly speaking, the results presented in this study are qualitatively robust to changes in system parameters and the form of the external forcing. Therefore we will present numerical results using the parameter choices

$$A = B = \iota = 1, \quad \alpha = 0, \quad p(x) = e^{-x^2}. \tag{6}$$

Choosing $\alpha = 0$ corresponds to a purely vertical substrate and produces more pronounced deflections, where the diffusive influence of transverse gravity has vanished (for example, see [44]). While the results are qualitatively the same for $\alpha > 0$, this choice allows us to focus on the suppression of the deflections due the control and not the transverse component of gravity.

Equipped with the optimal control problem (4), we now analyze solutions in two cases: first, the limit of vanishing normal capillarity, $\beta \to 0$, followed by the limit in which normal capillarity is non-negligible $\beta = \mathcal{O}(1)$. In each case our strategy is to formulate the adjoint problem, apply PMP to give the form of the optimal control, and present numerical solutions.

III. OPTIMAL COOLING WITHOUT NORMAL CAPILLARITY

For general theory and applications of optimal control theory, we refer the reader to [[43,45,46], and references therein] for the relevant technical conditions, proofs of PMP, and several examples. For optimal control problems that are linear in the control, we refer the reader to [47,48].

It is instructive to begin by considering a simplified form of problem (4) relevant in the limit where the third-order normal capillarity term is negligible, $\beta = 0$. The leading-order optimal cooling problem then reads

$$\min_{|u|\leqslant U} \frac{1}{2}\|\hbar\|_2^2, \tag{7a}$$

subject to the first-order deflection equation

$$\frac{d\hbar}{dx} = \frac{1}{\alpha\mathcal{Q}(\hbar) + B\mathcal{T}(\hbar)p}\left[\mathcal{Q}(\hbar)\left(1 - A\frac{dp}{dx}\right) - \mathcal{Q}(0) - B\mathcal{T}(\hbar)\left((\hbar + 1 + \iota)\frac{dp}{dx} + u\right)\right]. \tag{7b}$$

We transform Eq. (7b) into an autonomous system of two ODEs by introducing the auxiliary variable a and writing

$$\frac{d\hbar}{dx} = f(\hbar, a, u), \quad \frac{da}{dx} = 1, \tag{8a,b}$$

where the dynamics f are defined by

$$f(\hbar, a, u) = \frac{1}{\alpha\mathcal{Q}(\hbar) + B\mathcal{T}(\hbar)p(a)}\left[\mathcal{Q}(\hbar)\left(1 - A\frac{dp}{dx}(a)\right) - \mathcal{Q}(0) - B\mathcal{T}(\hbar)\left((\hbar + 1 + \iota)\frac{dp}{dx}(a) + u\right)\right] \tag{8c}$$

and are subject to the boundary condition

$$a(-X) = -X. \tag{9}$$

We now proceed to the adjoint formulation. Introducing the two-dimensional costate $\lambda = (\lambda_1, \lambda_2)$, the Hamiltonian H is given by

$$H(\hbar, a, \lambda, u) = \lambda_1 f(\hbar, a, u) + \lambda_2 + \frac{\lambda_0}{2}\hbar^2, \tag{10}$$

where λ_0 is a constant. The costate satisfies the adjoint equations

$$\frac{d\lambda_1}{dx} = -\lambda_1\frac{\partial f}{\partial \hbar} + \lambda_0\hbar, \quad \frac{d\lambda_2}{dx} = -\lambda_1\frac{\partial f}{\partial a}, \tag{11}$$

subject to the boundary conditions

$$\lambda_1(-X) = \lambda_1(X) = \lambda_2(X) = 0. \tag{12}$$

It follows from (11), (12), and the nontriviality of (λ_0, λ) guaranteed by PMP that $\lambda_0 \neq 0$. Problems satisfying this condition are referred to as normal, and by rescaling it may be assumed, without loss of generality, that $\lambda_0 = 1$.

With the forward problem (8) and (9) and the adjoint problem (10) to (12) in hand, we now apply PMP, which states that for any optimal state trajectory and optimal control pair there exists a nontrivial costate satisfying the adjoint equations such that the Hamiltonian is minimized for all admissible control values. That is, the optimal control u^* satisfies

$$H(\hbar, a, \lambda, u^*) = \min_{|u|\leqslant U} H(\hbar, a, \lambda, u). \tag{13}$$

The information in (13) characterizes the optimal control parametrically. When the Hamiltonian H is affine with respect to u, as it is in (10), since f given in (8c) is affine in u, the Hamiltonian may be written as

$$H(\hbar, a, \lambda, u^*) = u\phi(\hbar, a, \lambda) + \psi(\hbar, a, \lambda), \tag{14}$$

where $\phi = \partial H/\partial u$ and $\psi = H|_{u=0}$. It is then straightforward to see that the optimal control (dropping the asterisk for convenience) is given by

$$u = -U\,\mathrm{sgn}(\phi), \quad \text{where} \quad \phi \neq 0. \tag{15}$$

Since the optimal control switches sign with ϕ, it is commonly known as the switching function.

For problem (7), the switching function is given by

$$\phi = \frac{\partial H}{\partial u} = \lambda_1 \frac{\partial f}{\partial u} = \frac{-\lambda_1 B\mathcal{T}(\hbar)}{\alpha \mathcal{Q}(\hbar) + B\mathcal{T}(\hbar)p(a)}. \tag{16}$$

Since the flux functions $\mathcal{Q}$ and $\mathcal{T}$ are positive, it follows that $\mathrm{sgn}(\phi) = -\mathrm{sgn}(\lambda_1)$, and thus $u = U\,\mathrm{sgn}(\lambda_1)$ during intervals satisfying $\lambda_1 \neq 0$ (called nonsingular arcs). For intervals on which $\phi = 0$ identically, so-called singular arcs, we may determine the optimal control by observing that $\lambda_1 = 0$, and therefore its derivatives also vanish. From (11) we infer that $\hbar = 0$, in which case the optimal control is given by the unconstrained optimum (5). We have thus completely determined the optimal control parametrically, that is, as a function of the yet unknown state and costate:

$$u = \begin{cases} U\,\mathrm{sgn}(\lambda_1), & \lambda_1 \neq 0, \\ u_\infty, & \lambda_1 = 0. \end{cases} \tag{17}$$

We now check that singular arcs, if they exist, satisfy the strengthened generalized Legendre-Clebsch (GLC) condition [49]. The GLC condition is a second-order condition necessary for optimality. First we must calculate the local order of singular arcs, as detailed in [47]. Essentially, this involves finding the lowest-order derivative of the switching function ϕ which, when evaluated along a given singular arc, depends explicitly on the control u. The local order of the singular arc is defined as *half* the order of this lowest-order derivative. We find that on all singular arcs $d\phi/dx = 0$ and

$$(-1)\frac{\partial}{\partial u}\left(\frac{d^2\phi}{dx^2}\right) = \left(\frac{B\mathcal{T}(0)}{\alpha \mathcal{Q}(0) + B\mathcal{T}(0)p(a)}\right)^2 > 0. \tag{18}$$

Therefore the local order of all singular arcs is 1, and the strengthened GLC condition for singular arcs of order 1 [requiring the left-hand side of (18) to be positive] is satisfied.

With the parametric form of the optimal control (17), we seek numerical solutions of the optimal control problem (7). The literature on numerical approaches to optimal control problems is vast. We provide a brief outline in Appendix B, focusing on the details most relevant to our problem. In summary, two central approaches are (i) indirect methods, which seek to solve the (discretized) ODEs describing first-order optimality (that is, given by PMP); and (ii) direct methods, which seek to solve a discretization of the constrained optimization problem. These may be seen as (i) optimize–then–discretize versus (ii) discretize–then–optimize.

Solutions of problem (7) using indirect and direct approaches are shown in Fig. 2(a), where we find good agreement between the two methods. The rest of the numerical results presented in this paper employ the direct approach, since the sensitivity of the indirect approach to the initial guess is prohibitive when the switching structure is sufficiently dense [50], and the instability of the forward problem as an initial value problem only compounds the difficulty. The direct approach does not rely on the adjoint formulation; nevertheless, the insights provided by the adjoint problem alongside PMP are invaluable. Firstly, the parametric form of the optimal control shows that it belongs to the subset of functions that (piecewise) coincide with either the unconstrained optimum u_∞ or the control bounds $\pm U$. This provides a sanity check for any numerical solution, including direct methods. More importantly, we will see that the analytic information from the adjoint formulation and PMP will prove indispensable in understanding the numerical solution structure.

In Fig. 2(b) we plot the solutions for various control bounds U. The control is of the form predicted by PMP (17): for small enough U, the optimal control u is bang-bang [that is, switches between values $\pm U$ as per (15)] in a region around the origin where $u_\infty > U$. Beyond this region the control coincides with the unconstrained optimum on singular arcs and the deflections vanish. For larger U, an additional inner region emerges in close proximity to the origin where the control is singular, coinciding with the unconstrained optimal control u_∞. Outside this local inner region it takes on a constant value, and finally, singular arcs extend beyond the bang-bang region to the far field, just as for smaller U. The results depicted in Fig. 2(b) confirm the claim made in Sec. II that deflections are suppressed beyond a neighborhood of the origin.

With greater control (increasing U) the deflections diminish. The force of gravity causes the upstream deflection to be significantly more pronounced than its downstream counterpart and is also the reason why the control switch (from $u = -U$ to $u = U$ for the bang-bang controls with small U, or the center of the inner singular region for larger U) occurs downstream of the origin.

We now reinstate normal capillarity by considering the fully physical case of $\beta = \mathcal{O}(1)$ and proceed with an analogous approach. The results transpire to be remarkably different from those for the first-order problem, uncovering an interesting phenomenon regarding the transition between nonsingular and singular arcs.

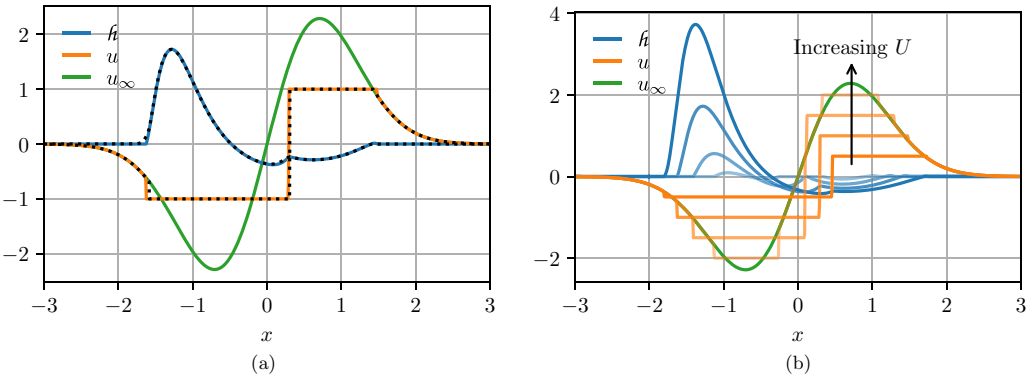

FIG. 2. Solutions of the first-order problem (7) when $\beta = 0$ (a) using the direct (solid curves) and indirect (broken curves) numerical approaches for $U = 1$; (b) for control bounds $U \in \{0.5, 1, 1.5, 2\}$ using the direct approach. Other parameters are defined in (6). For the direct approach, $N = 1000$ equispaced grid points were used.

IV. REINSTATING NORMAL CAPILLARITY

In this section we reinstate normal capillarity by taking $\beta = \mathcal{O}(1)$. All numerical results will employ the value $\beta = 1$, which is equivalent to rescaling the system length on the capillary length scale (given at the end of Appendix A).

We transform Eq. (1) into a four-dimensional autonomous system by introducing auxiliary variables a_1, a_2, and a_3, and writing

$$\frac{d\hbar}{dx} = a_1, \quad \frac{da_1}{dx} = a_2, \quad \frac{da_2}{dx} = f(\hbar, a_1, a_3, u), \quad \frac{da_3}{dx} = 1, \tag{19a-d}$$

where the dynamics f satisfy

$$\beta f = \frac{Q(0)}{Q(\hbar)} - \left(1 - A\frac{dp}{dx}(a_3) - \alpha\, a_1\right) + \frac{B\mathcal{T}(\hbar)}{Q(\hbar)}\left((\hbar + 1 + \iota)\frac{dp}{dx}(a_3) + a_1 p(a_3) + u\right), \tag{19e}$$

and we impose the boundary condition

$$a_3(-X) = -X. \tag{20}$$

We construct the adjoint problem by defining the Hamiltonian as

$$H = \lambda_1 a_1 + \lambda_2 a_2 + \lambda_3 f(\hbar, a_1, a_3, u) + \lambda_4 + \frac{1}{2}\hbar^2, \tag{21}$$

where, as in the previous case, it may be shown that the problem is normal. The four-dimensional costate λ satisfies the adjoint equations

$$\frac{d\lambda_1}{dx} = -\lambda_3\frac{\partial f}{\partial \hbar} - \hbar, \quad \frac{d\lambda_3}{dx} = -\lambda_2, \quad \frac{d\lambda_2}{dx} = -\lambda_1 - \lambda_3\frac{\partial f}{\partial a_1}, \quad \frac{d\lambda_4}{dx} = -\lambda_3\frac{\partial f}{\partial a_3}, \tag{22}$$

subject to the boundary conditions

$$\lambda_1(-X) = \lambda_2(-X) = \lambda_3(-X) = 0, \quad \lambda_1(X) = \lambda_2(X) = \lambda_3(X) = \lambda_4(X) = 0. \tag{23}$$

The problem (4) is affine in the control, with the switching function given by

$$\phi = \frac{\partial H}{\partial u} = \frac{\lambda_3 B\mathcal{T}(\hbar)}{\beta Q(\hbar)}. \tag{24}$$

As before, $Q, \mathcal{T} > 0$, and we deduce that singular arcs (intervals on which $\phi \equiv 0$) are characterized by the equalities $\lambda_1 = \lambda_2 = \lambda_3 = \hbar = a_1 = a_2 = 0$, from which it follows that the optimal control will take its unconstrained value u_∞. Therefore the application of PMP determines the optimal control parametrically, namely,

$$u = \begin{cases} -U\,\mathrm{sgn}(\lambda_3), & \lambda_3 \neq 0, \\ u_\infty, & \lambda_3 = 0. \end{cases} \tag{25}$$

We now check the GLC condition. We find that for $i = 1, \ldots, 5$, the expressions $d^i\phi/dx^i$ do not depend explicitly on u along singular arcs, while

$$(-1)^3\frac{\partial}{\partial u}\left(\frac{d^6\phi}{dx^6}\right) = \left(\frac{B\mathcal{T}(0)}{\beta Q(0)}\right)^2 > 0, \tag{26}$$

from which we conclude that the local order of all singular arcs is 3, and trajectories along singular arcs satisfy the strengthened GLC condition.

Using the direct numerical method detailed in Appendix B, we solve the full optimal control problem (4) with normal capillarity reinstated $\beta = 1$. We plot the numerical solution in Fig. 3(a) with bound $U = 1$. The film deflections $\hbar$ (solid blue curve) are significantly reduced when compared with the uncontrolled film (dashed blue curve). We see the optimal control appears to be of the form predicted by PMP in (25): bang-bang (with many switches) in a nonsingular region around the origin, and coinciding with the unconstrained optimum u_∞ beyond this region. Despite the optimal control form (25) being analogous to its first-order counterpart (17), the computed control in Fig. 3(a) looks stunningly different from those in Fig. 2, switching many more times within the more extensive bang-bang region. To understand what is happening we revisit an oft-forgotten optimal control phenomenon: chattering.

A brief historical perspective and a complete exposition are provided in Appendix C. It turns out that an optimal control may switch (between its upper and lower bound) an infinite

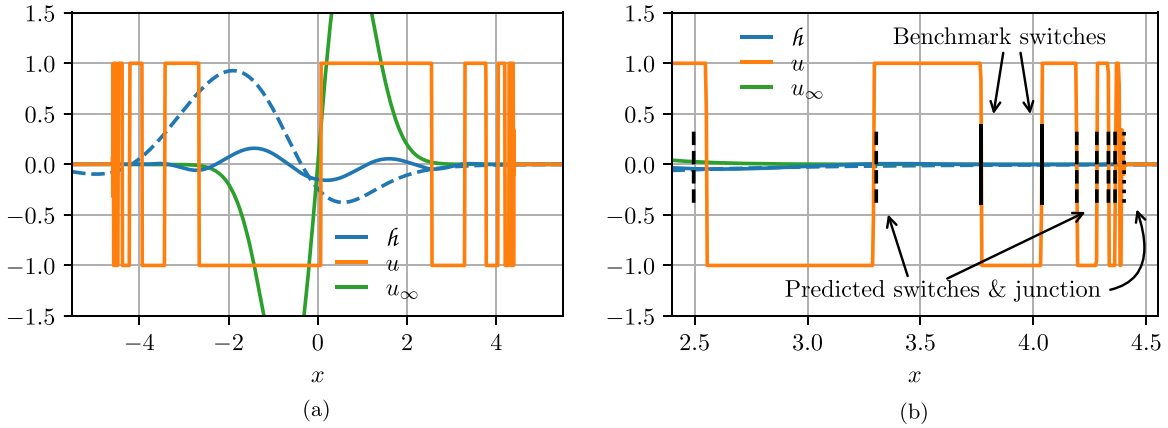

FIG. 3. (a) Optimal solution of problem (4) for $\beta = U = 1$ with $N = 10^4$ equispaced grid points, and the parameters defined in (6). For the purpose of comparison, the dashed curve shows the uncontrolled film profile, $\hbar$ for $U = 0$. (b) A section of (a), where $(x_0, x_1) \approx (3.77, 4.04)$ are the benchmark switching points (marked by solid black lines), and the geometric ratio $J \approx 0.575\,736$ is used to predict adjacent switching points (dashed lines), as well as the junction point (dotted line).

number of times on a nonsingular arc in the vicinity of a junction point (a point where a nonsingular arc meets a singular arc). This infinite switching is referred to as chattering. An analysis local to the junction point reveals that the switching function admits approximately self-similar solutions, which results in a geometric sequence of switching points with ratio J, which is a root of a particular polynomial and thus obtainable numerically. Therefore we may take any two adjacent points as a benchmark and predict the entire infinite sequence. In Fig. 3(b) we zoom in on a section of Fig. 3(a) and take the two adjacent switching points $(x_0, x_1) \approx (3.77, 4.04)$ as the benchmark interval (solid vertical lines). Using $J \approx 0.575\,736$ calculated in Appendix C, we predict adjacent switching points (dashed lines) as well as their accumulation point, the junction point (dotted line). For switching points beyond the benchmark interval $x > x_1$, including the junction point, we find excellent agreement (we mark only four such switches because the separation is no longer clearly visible). Switching points preceding the benchmark interval $x < x_0$ show slightly diminishing agreement as the approximation [see (C2)] breaks down towards the origin as we leave the vicinity of the junction point. We conclude that the self-similar structure derived in Appendix C accurately characterizes the chattering structure. Having pinned down the chattering behavior, we proceed to consider various approaches to tame the chattering.

V. REGULARIZING THE CHATTERING

The optimal control calculated in Sec. IV exhibits chattering, characterized by an infinite number of switches in the vicinity of the junction joining nonsingular and singular arcs. In practice, such a cooling profile cannot be realized, and we seek a practical regularization.

The direct numerical method discretizes the control and thus cannot switch infinitely many times, offering one such regularization. However, the switching still occurs at intolerably high frequency. While courser discretization would suppress this, we seek a more robust formulation that offers more freedom in the choice of switching points.

One successful approach taken in the literature [50] is to add an additional penalty term to the objective function so that it takes the form

$$\frac{1}{2}\|\hbar\|_2^2 + \varepsilon\,\mathrm{TV}(u), \tag{27}$$

where TV denotes the total variation and ε is a small parameter. Optimal solutions will be those of bounded variation and thus can switch only a finite number of times. As $\varepsilon \to 0$, the number of switches diverges and thus the parameter $\varepsilon > 0$ does not generate a space of solutions that are feasibly engineered.

Instead, we propose a more practical approach of keeping the generic bang-bang or unconstrained form (25) while predetermining a finite number of switches n. This reduces the problem to an n-dimensional optimization problem of determining the optimal switching locations.

In the case of $n = 3$, we denote the switching locations by $x_\mathrm{L} < x_\mathrm{C} < x_\mathrm{R}$, where the control is given by

$$u(x) = \begin{cases} u_\infty(x), & x < x_\mathrm{L}, \\ -U, & x_\mathrm{L} \leqslant x < x_\mathrm{C}, \\ U, & x_\mathrm{C} \leqslant x < x_\mathrm{R}, \\ u_\infty(x), & x \geqslant x_\mathrm{R}. \end{cases} \tag{28}$$

The optimization problem is now reduced to minimizing the objective over the finite-dimensional $(x_\mathrm{L}, x_\mathrm{C}, x_\mathrm{R})$ parameter space. This problem is numerically tractable using general-purpose optimization tools. In Fig. 4 we show the objective function on subspaces of the parameter space. There is a local minimum at $(x_\mathrm{L}, x_\mathrm{C}, x_\mathrm{R}) \approx (-2.30, 0.07, 2.14)$ where the objective function takes the value of $\|\hbar\|_2 \approx 0.240$. The high-frequency switching solution in Fig. 3 achieves $\|\hbar\|_2 \approx 0.217$, showing that the relative increase in objective for the significantly simpler control is around 10% but still significantly improved from the value of $\|\hbar\|_2 \approx 1.276$ attained in the uncontrolled case. The deflection profiles for both of these optima are shown in Fig. 5 along with the uncontrolled deflections. The two optima are very similar in comparison to the uncontrolled profile.

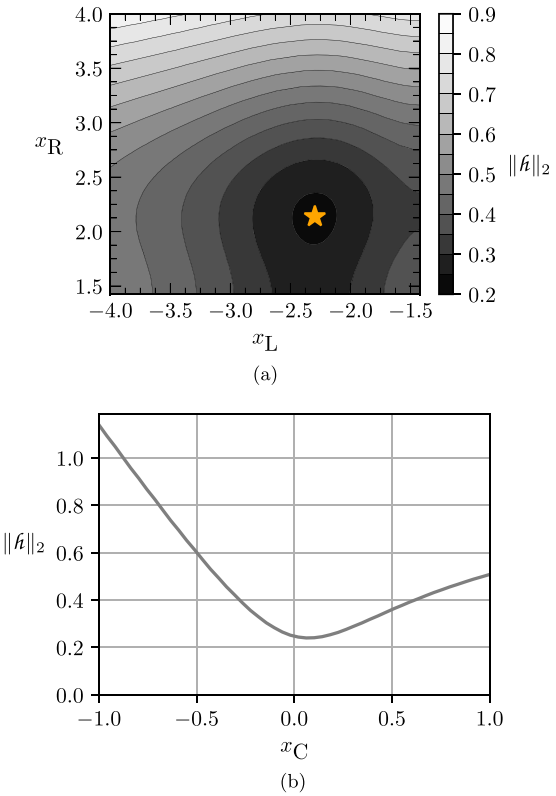

FIG. 4. Value of the objective function $\|\hbar\|_2^2$ when $\beta = U = 1$, on subspaces of the (x_L, x_C, x_R) parameter space in the vicinity of the local minimum $(x_L, x_C, x_R) \approx (-2.30, 0.07, 2.14)$ marked on the contour plot in (a) by a star while (a) varying x_L and x_R, keeping $x_C = 0.07$, and (b) varying x_C, keeping $(x_L, x_R) = (-2.30, 2.14)$. All other parameters are defined in (6).

A straightforward physical explanation of the convex optimality structure of Fig. 4 is available by exploring the deflection profiles while varying x_L and x_R independently, as shown in Fig. 6. In Fig. 6(a) we see that the effect of deviations in the upstream control boundary x_L from its optimal

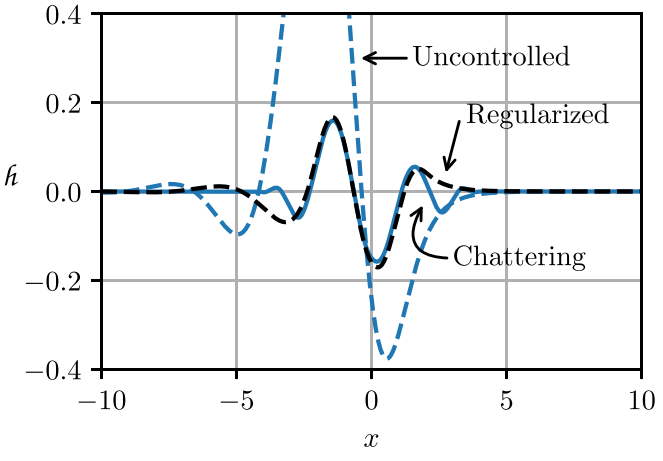

FIG. 5. Deflection profiles $\hbar$ when $\beta = 1$ for the chattering optimum ($U = 1$, solid blue curve), the three-switch regularization ($U = 1$, dashed black curve), and the uncontrolled profile ($U = 0$, blue dashed curve). All other parameters are given in (6).

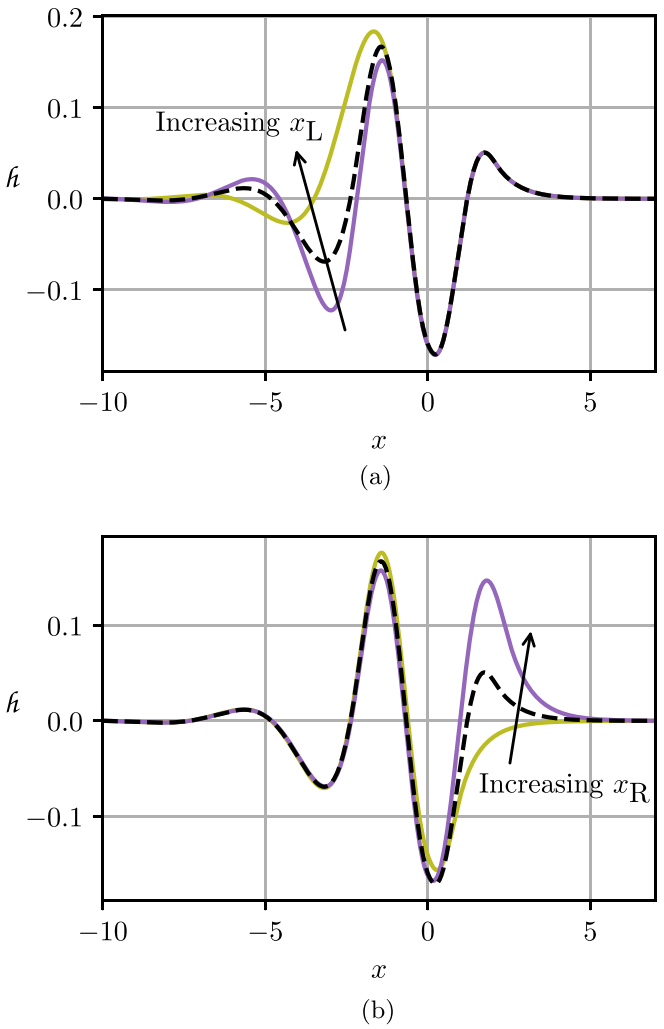

FIG. 6. Deflection profiles $\hbar$ [solutions of (4) with $\beta = U = 1$ and other parameters defined in (6)] using the three-switch control (28) with $x_C = 0.07$ and (a) $x_R = 2.14$, $x_L \in \{-1, -2.30, -2.5\}$; and (b) $x_L = -2.30$, $x_R \in \{1, 2.14, 2.5\}$. The local minimum deflection profile is drawn as a black dashed curve.

value lead to amplified upstream features: a peak for $x_L = -1$ (the yellow curve) and a trough for $x_L = -2.5$ (the purple curve). Similarly, in Fig. 6(b) we observe how changes to the downstream control boundary location x_R alter downstream deflection features: increasing x_R amplifies the downstream peak, while decreasing x_R affects more moderate change [visible also in Fig. 4(a)]. We deduce that localized control changes drive localized deflections, with deviations from the optimum becoming progressively worse as larger deformations are induced.

We conclude with remarks regarding alternative objective functions. When other L^p norms are used as the objective functional we obtain comparable results to those presented in this section. While it might be tempting to think that derivative information of $\hbar$ is missing from the formulation, it transpires that employing a Sobolev norm, where we minimize, say, $\|\hbar\|_2^2 + \|d\hbar/dx\|_2^2$, does not prevent chattering, nor does an L^2 norm on the control [50].

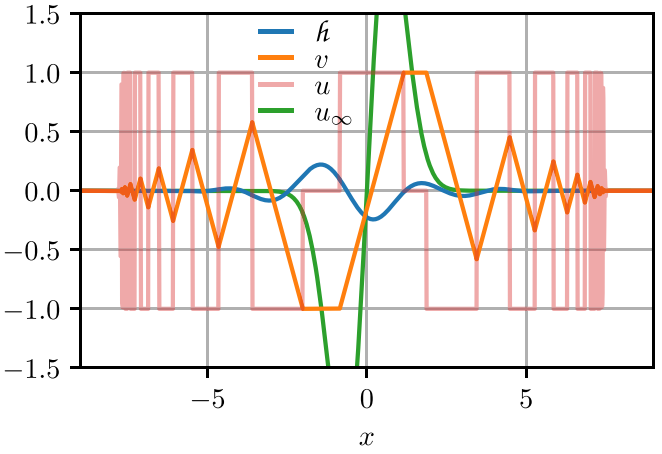

FIG. 7. Optimal solution of the augmented system obtained from problem (4) with $\beta = 1$ by considering u as a state variable governed by the control v via $du/dx = v$, and imposing $|u|, |v| \leqslant 1$, with $N = 5000$ equispaced grid points, and the parameters defined in (6).

The chattering control has a derivative of Dirac δ masses at switching points. Therefore it might be tempting to think that we can suppress chattering if we could bound the control derivative. This can be achieved by employing higher-order control (a technique common in feedback control [51]). For the sake of concreteness, denoting the autonomous, controlled dynamics and associated constraints by $dy/dx = f(y, u)$ and $|u| \leqslant U$, respectively, we consider the augmented dynamics $dy/dx = f(y, u), du/dx = v$, along with the constraints $|u| \leqslant U$ and $|v| \leqslant V$. While u remains the input to the system that influences the dynamics and thus must respect the bound U, we interpret it as a state variable (with a state constraint) since we no longer fix u directly but instead fix the control v and u is determined from the dynamics. This is a higher-order control because instead of controlling the second argument of the dynamics $f(y, \cdot)$, we effectively control, and can thus bound, its derivative.

There is an inherent tradeoff in choosing the new control bound V. In the limit as $V \to \infty$ we converge to the original system, and thus to effectively suppress chattering we need a relatively small value for V. However, decreasing V more tightly constrains the control and thus results in increased penalties. We show the solution for $U = V = 1$ in Fig. 7, where we see that the chattering persists but is modulated by a linear envelope. (Proceeding to higher order produces polynomial envelopes of higher degree; however, the chattering persists.) The optimal solution in Fig. 7 achieves $\|\bar{h}\|_2 \approx 0.321$, almost 50% worse than the optimum and vastly more difficult to engineer than the regularized optimum. We deduce that this poor performance is the result of the bounded derivative not providing sharp control, especially in the vicinity of the origin.

VI. SUMMARY

In this paper we consider the steady free-surface flow of a thin film of incompressible, viscous fluid along a substrate, under the influence of gravity and an external source of localized momentum and heat flux, and exposed to an active cooling mechanism from underneath the substrate. We are concerned with the case where the free-surface deformations caused by the external source are undesirable and pose the optimal control problem of finding the cooling profile that minimizes these deflections (where the active cooling mechanism is subject to temperature gradient constraints). We investigate the problem in two limits, with and without the normal component of capillary stress at the fluid interface. The striking difference between the results highlights the importance of normal capillarity in the optimal control problem.

In both cases numerical solutions show that the optimal control succeeds in suppressing all deflections sufficiently far from regions of peak external forcing. However, when normal capillarity is present the solution is remarkably different: the control chatters at junctions joining the nonsingular arcs (where deflections are nonzero) and singular arcs (where deflections are completely suppressed), that is, the control switches from its upper bound to its lower bound an infinite number of times in a finite vicinity of the junction.

To explore the switching, we turn to Pontryagin's maximum principle and the adjoint problem, from which we derive a nonlinear ODE whose solution approximates the switching function. We exploit a symmetry of this nonlinear ODE to construct self-similar solutions whose changes in sign accurately predict the "fractal" switching structure.

For the purposes of practical implementation, several regularization approaches to suppress the chattering are discussed. Taking only a known, finite number of switches is a simple approach that has several key advantages. Firstly, of key industrial importance, the simple control structure imposed ensures that the optimal strategy will be practical to engineer. Secondly, given a forward model, optimizing the design reduces to solving a classical optimization problem where generic optimization tools are effective and widely available. Finally, in terms of the objective function, the price for deviating from the unregularized optimum can be kept small. An example with typical parameters shows that having just three switches results in only slightly worse performance than the optimal strategy. The cooling strategy obtained with this regularization is essentially uniform beyond a neighborhood of the origin, in which the substrate temperature decreases around a point slightly downstream of the origin.

While numerical results are presented only for hydrodynamic flow, we reiterate that the results are universal and remain qualitatively descriptive for similar flow regimes, such as magnetohydrodynamic flow. We restrict our attention to the steady-state problem formulation, which motivates a more complete stability analysis of the three-dimensional hydrodynamic (and magnetohydrodynamic) problem. In the dynamic setting, unsteady forcing can excite resonant free-surface deflections [38]. How this affects the optimal control (and in particular, the chattering) would be a fascinating topic for future work. Further questions regarding the analysis and characterization of the transition between the nonchattering and chattering regimes could also shed more light on this fascinating phenomenon.

ACKNOWLEDGMENTS

I would like to thank Richard Tockar and Mark Ganz for entertaining discussions that sparked my interest in this topic, as well as Prof. Peter D. Howell for helpful suggestions. This paper was based on work supported by the EPSRC Centre For Doctoral Training in Industrially Focused Mathematical Modelling (Grant No. EP/L015803/1) in collaboration with Tokamak Energy.

APPENDIX A: DERIVATION OF THE THIN-FILM EQUATION

We present a brief derivation of the thin-film equation (1) and 2 in the main text governing the evolution of the fluid's free surface. We refer the reader to [52] for an extensive treatment of the relevant equations and boundary conditions governing fluid motion.

We consider the two-dimensional configuration illustrated in Fig. 1 of the main text, where (x, y) are Cartesian coordinates. The fluid occupies the region $0 < y < h(x,t)$, where t denotes time and $h(x,t)$ denotes the fluid thickness. The velocity $\boldsymbol{v}(x,y,t)$ and pressure $p(x,y,t)$ satisfy the incompressible Navier-Stokes equations describing the conservation of mass and momentum, namely,

$$\boldsymbol{\nabla}\cdot\boldsymbol{v} = 0, \tag{A1a}$$

$$\rho\left(\frac{\partial \boldsymbol{v}}{\partial t} + (\boldsymbol{v}\cdot\boldsymbol{\nabla})\boldsymbol{v}\right) = -\boldsymbol{\nabla}p + \rho\nu\boldsymbol{\nabla}^2\boldsymbol{v} + \rho\boldsymbol{g}, \tag{A1b}$$

where $\boldsymbol{g}$ is gravitational acceleration, ρ is the fluid density, and ν its kinematic viscosity. We assume that these quantities are constant in the temperature range of interest.

The conservation of energy within the fluid is described by an advection-diffusion equation governing the evolution of temperature $T(x,y,t)$, namely,

$$\frac{\partial T}{\partial t} + \boldsymbol{v}\cdot\boldsymbol{\nabla}T = \kappa\boldsymbol{\nabla}^2 T, \tag{A2}$$

where κ denotes the thermal diffusivity of the fluid. The substrate occupies the region $-h^{\mathrm{s}} < y < 0$, where h^{s} denotes the constant substrate thickness, in which the temperature, denoted T^{s}, evolves according to

$$\frac{\partial T^{\mathrm{s}}}{\partial t} = \kappa^{\mathrm{s}}\boldsymbol{\nabla}^2 T^{\mathrm{s}}, \tag{A3}$$

with κ^{s} denoting the thermal diffusivity of the substrate.

We now describe the boundary conditions at each material interface. Motivated by the fusion context in which there is a vacuum above the fluid, we assume that the ions impact, and are absorbed by, the fluid (as in in an attached divertor regime), conferring a flux of momentum [53] and heat [37]. These are captured at the interfacial boundary conditions due to the fact that the ions have energies on the order of $\mathcal{O}(100)$ eV [54], which result in their penetrating only the tiniest fraction of the fluid film [55]. Tangential stresses due to the impinging jets have been neglected following Refs. [53,56].

At the vacuum-fluid interface, the free surface $y = h(x,t)$, we impose the kinematic condition, normal and tangential stress balances, and the normal heat flux condition, which take the forms

$$\frac{1}{\sqrt{1+(\partial h/\partial x)^2}}\frac{\partial h}{\partial t} = \boldsymbol{v}\cdot\boldsymbol{n}, \tag{A4a}$$

$$\rho\nu[\left(\boldsymbol{\nabla}\boldsymbol{v} + (\boldsymbol{\nabla}\boldsymbol{v})^T\right)\cdot\boldsymbol{n}]\cdot\boldsymbol{n} = p - P - \gamma\,(\boldsymbol{\nabla}\cdot\boldsymbol{n}), \tag{A4b}$$

$$\rho\nu[\left(\boldsymbol{\nabla}\boldsymbol{v} + (\boldsymbol{\nabla}\boldsymbol{v})^T\right)\cdot\boldsymbol{n}]\cdot\boldsymbol{t} = -\frac{d\gamma}{dT}\boldsymbol{\nabla}T\cdot\boldsymbol{t}, \tag{A4c}$$

$$k\boldsymbol{\nabla}T\cdot\boldsymbol{n} = H, \tag{A4d}$$

where $\boldsymbol{n}$ and $\boldsymbol{t}$ are, respectively, the (upward) normal and tangential unit vectors, γ is the surface tension of the fluid, $P(x)$ and $H(x)$ are, respectively, the pressure imposed and heat transferred to the fluid from the external source impinging upon the fluid, and k is the thermal conductivity of the fluid.

At the fluid-substrate interface, we impose a no-slip boundary condition, along with continuity of temperature and thermal flux, which take the forms

$$\boldsymbol{v} = 0, \quad T = T^{\mathrm{s}}, \quad k\boldsymbol{\nabla}T\cdot\boldsymbol{n} = k^{\mathrm{s}}\boldsymbol{\nabla}T^{\mathrm{s}}\cdot\boldsymbol{n}, \tag{A5a-c}$$

with k^{s} denoting the thermal conductivity of the substrate.

Finally, we represent the active cooling mechanism via a Dirichlet temperature boundary condition on the underside of the substrate, $y = -h^{\mathrm{s}}$, namely,

$$T^{\mathrm{s}} = T^{-}(x). \tag{A6}$$

Writing $\boldsymbol{v} = (v, w)$, where v and w denote the horizontal and vertical velocity components, respectively, we integrate (A1a) and impose (A4a) and (A5a) to obtain a relation describing the net conservation of mass:

$$\frac{\partial h}{\partial t} + \frac{\partial}{\partial x}\left(\int_0^h v\,\mathrm{d}y\right) = 0. \tag{A7}$$

Relation (A7) replaces the need to solve for the vertical component of the velocity w. Given the horizontal velocity component v, Eq. (A7) provides the free-surface dynamics.

We now proceed to nondimensionalize the governing equations and boundary conditions Eqs. (A1)–(A6). Our aim is to apply the lubrication approximation to exploit the physically relevant limit in which the film is thin compared to the substrate length and provide a leading-order asymptotic approximation for the horizontal velocity and temperature. This leading-order solution, in conjunction with (A7), provides a leading-order equation governing the free-surface evolution.

We scale our dimensional variables with characteristic magnitudes via

$$\begin{aligned}
&x = \mathcal{L}x', \quad y = \epsilon\mathcal{L}y', \quad t = \frac{\mathcal{L}}{\mathcal{U}}t',\\
&v = \mathcal{U}v', \quad w = \epsilon\mathcal{U}w', \quad p = \frac{\rho\nu\mathcal{U}}{\epsilon^2\mathcal{L}}p',\\
&h = \epsilon\mathcal{L}h', \quad P = P_0 p, \quad T = T_0 + \frac{\epsilon\mathcal{L}H_0}{k}T',\\
&h^{\mathrm{s}} = \epsilon\mathcal{L}h^{\mathrm{s}\prime}, \quad H = H_0 p, \quad T^{-} = T_0 + \frac{\epsilon\mathcal{L}H_0}{k}T^{-\prime},
\end{aligned} \tag{A8}$$

where $\mathcal{L}$, $\mathcal{U}$, P_0, and H_0 denote characteristic scales of length, velocity, externally applied pressure, and thermal flux, ϵ

TABLE I. Dimensionless quantities and the asymptotic limits of interest.

Dimensionless quantity	Notation	Description	Asymptotic limit
Flow aspect ratio	$\epsilon = \frac{\mathcal{H}}{\mathcal{L}}$	$\frac{\text{Fluid thickness}}{\text{Divertor extent}}$	$\epsilon \ll 1$
Reynolds number	$\mathrm{Re} = \frac{\epsilon \mathcal{U}\mathcal{L}}{\nu}$	$\frac{\text{Inertia}}{\text{Viscosity}}$	$\epsilon\,\mathrm{Re} \ll 1$
Péclet number	$\mathrm{Pe} = \frac{\epsilon \mathcal{U}\mathcal{L}}{\kappa}$	$\frac{\text{Advection}}{\text{Thermal diffusion}}$	$\epsilon\,\mathrm{Pe}, \epsilon\,\mathrm{Pe}\,\kappa/\kappa^{\mathrm{s}} \ll 1$
Bond number	$\mathrm{Bo} = \frac{\epsilon^2 \mathcal{L}^2 \rho \lvert \boldsymbol{g} \rvert \sin\theta}{\gamma}$	$\frac{\text{Gravity}}{\text{Surface tension}}$	$\mathrm{Bo} = \mathcal{O}(\epsilon^3)$ and $\mathrm{Bo} \gg \epsilon^3$
Marangoni number	$\mathrm{Ma} = -\frac{d\gamma}{dT}\frac{\epsilon^2 \mathcal{L}^2 H_0}{\rho \nu \kappa k}$	$\frac{\text{Thermocapillary}}{\text{Thermal diffusion}}$	$\epsilon\,\mathrm{Ma}\,/\,\mathrm{Pe} = \mathcal{O}(1)$

denotes the small aspect ratio of the flow (the ratio of the typical film thickness to the substrate length), and $p(x)$ represents the profile of the pressure and heat source, that is, the spatial distribution of their magnitude, being localized in the vicinity of the origin and decaying in the far field. We assume that these emanate from the same source and thus model them with different magnitudes but the same spatial profile p. The temperature scale reflects the absolute temperature reference T_0 dictated by the cooling mechanism, say, $T_0 = \min_x T^-(x)$, and the temperature jump, dictated by the external heating and thermal conductivity of the fluid. We nondimensionalize T^{s} identically to T. We henceforth drop the primes to reduce clutter.

We may deduce the gravity-driven velocity scale by considering a dominant balance between gravitational and viscous forces in (A1b), from which we find that

$$\mathcal{U} = \frac{\epsilon^2 \mathcal{L}^2 \lvert \boldsymbol{g} \rvert \sin\theta}{\nu}. \tag{A9}$$

We are interested in the case of a thin film, where the aspect ratio is small, $\epsilon \ll 1$, and proceed to derive a reduced model in the asymptotic limit as $\epsilon \to 0$. We are interested in the distinguished limit in which $k/k^{\mathrm{s}} = \mathcal{O}(1)$, while we assume that $\epsilon\,\mathrm{Re}$, $\epsilon\,\mathrm{Pe}$, and $\epsilon\,\mathrm{Pe}\,\kappa/\kappa^{\mathrm{s}}$ are all negligible as $\epsilon \to 0$, and we neglect terms of these orders, or higher, in the leading-order system, as is typical in lubrication theory. The Reynolds and Péclet numbers, Re and Pe, respectively, are dimensionless quantities defined in Table I. We retain all other terms, for instance, we consider the distinguished limit where $\theta = \mathcal{O}(\epsilon)$, whereby we retain the transverse contribution of gravity.

To justify these asymptotic limits concretely, we consider characteristic orders of magnitude relevant to the fusion context. To this end we refer the reader to [57,58] for a compilation of the physical properties of liquid lithium and stainless steel, a leading candidate for liquid metal and substrate material in fusion applications [4,6,61–64]. For the typical film dimensions as well as heat flux and pressure magnitudes and profiles, we refer to the relevant modeling [6,53,59] and experimental [37,60] literature.

In Table II we tabulate the fusion-relevant physical parameters necessary to calculate the dimensionless limits of interest in Table I. We find that the reduced Reynolds number $\epsilon\,\mathrm{Re} \approx 10^{-3}$ and the scaled Péclet number $\epsilon\,\mathrm{Pe} \approx 10^{-4}$ are negligibly small. We deduce that the flow is noninertial. The normal capillary coefficient $\epsilon^3/\,\mathrm{Bo} \approx 10^{-5}$ is small, however, since it is the coefficient of a high-order derivative it becomes relevant in the presence of small-scale disturbances. The thermocapillary contribution $\epsilon\,\mathrm{Ma}\,/\,\mathrm{Pe}$ lies between $(10^{-2}, 10^{-1})$.

We assume that, in the temperature range of interest, the physical properties of the fluid and substrate are constant to leading order. This assumption is physically reasonable since the external heat source is localized [37] and the film has a small aspect ratio; therefore, even though temperature gradients might be large, the change in absolute temperature is limited. In fact, the dimensional temperature scale in (A8) is on the order of 10 K.

Assuming that both the surface tension and its gradient are constant to leading order is justified when surface tension varies sufficiently linearly in the temperature range of interest, and the variation does not have a significant effect on the surface tension magnitude, that is, the ratio $\gamma/(d\gamma/dT)$ is significantly larger than the temperature variation in the system. For liquid lithium the linearity assumption is exceedingly accurate, and the above ratio is on the order of 10^4 K, far exceeding the magnitude of the temperature scale [58].

With the leading-order reductions physically motivated, we proceed to write down the leading-order system. Equations (A1b) and (A2) in the fluid layer, $0 < y < h$, take the leading-order dimensionless forms

$$\frac{\partial p}{\partial x} = \frac{\partial^2 v}{\partial y^2} + 1, \quad \frac{\partial p}{\partial y} = -\epsilon \cot\theta, \quad \frac{\partial^2 T}{\partial y^2} = 0, \tag{A10a-c}$$

TABLE II. Typical dimensional parameter values [6,57–60].

Dimensional quantity	Symbol	Value
Film thickness	$\mathcal{H}$	10^{-4} m
Divertor extent	$\mathcal{L}$	0.1 m – 1 m
Kinematic viscosity	ν	$10^{-6}\ \mathrm{m}^2/\mathrm{s}$
Thermal conductivity (fluid)	k	50 W/ m K
Thermal conductivity (substrate)	k^{s}	20 W/ m K
Thermal diffusivity (fluid)	κ	$10^{-5}\ \mathrm{m}^2/\mathrm{s}$
Thermal diffusivity (substrate)	κ^{s}	$5 \times 10^{-6}\ \mathrm{m}^2/\mathrm{s}$
Density	ρ	$500\ \mathrm{kg/m}^3$
Thermal load	H_0	$10^7\ \mathrm{W/m}^2$
Surface tension	γ	0.5 N/m
Surface tension gradient	$-d\gamma/dT$	10^{-4} N m/K

while in the substrate, $-h^{\mathrm{s}} < y < 0$, the leading-order temperature is governed by

$$\frac{\partial^2 T^{\mathrm{s}}}{\partial y^2} = 0. \tag{A11}$$

At the free surface, $y = h$, boundary conditions (A4) take the leading-order forms

$$p - Ap + \frac{\epsilon^3}{\mathrm{Bo}} \frac{\partial^2 h}{\partial x^2} = 0, \tag{A12a}$$

$$\frac{\partial v}{\partial y} + B\left(\frac{\partial T}{\partial x} + \frac{\partial h}{\partial x}\frac{\partial T}{\partial y}\right) = 0, \tag{A12b}$$

$$\frac{\partial T}{\partial y} = p, \tag{A12c}$$

where we introduce the dimensionless coefficients A and B, representing the significance of the pressure and thermocapillarity, respectively, defined by

$$A = \frac{\epsilon^2 \mathcal{L} P_0}{\rho \nu \mathcal{U}}, \quad B = \frac{\epsilon\,\mathrm{Ma}}{\mathrm{Pe}}, \tag{A13}$$

with Bo and Ma denoting the Bond and Marangoni numbers defined in Table I.

We look to retain the thermocapillary flow and the effects of both externally applied sources, and thus consider the distinguished limit in which $A = \mathcal{O}(1)$ and $B = \mathcal{O}(1)$ as $\epsilon \to 0$. At the fluid-substrate interface, $y = 0$, the boundary conditions (A5) become

$$v = 0, \quad T = T^{\mathrm{s}}, \quad k\frac{\partial T}{\partial y} = k^{\mathrm{s}}\frac{\partial T^{\mathrm{s}}}{\partial y}. \tag{A14a-c}$$

Finally, on the lower side of the substrate, $y = -h^{\mathrm{s}}$, the cooling profile (A6) is imposed:

$$T^{\mathrm{s}} = T^{-}. \tag{A15}$$

To begin solving the leading-order system (A10) to (A12), (A14)), and (A15), we first integrate the decoupled temperature equations (A10c) and (A11), imposing boundary conditions (A12c), (A14b–c), and (A15), to find that

$$T(x, y) = p(x)(y + \iota) + T^{-}(x), \tag{A16a}$$

$$T^{\mathrm{s}}(x, y) = \frac{k}{k^{\mathrm{s}}} p(x)(y + h^{\mathrm{s}}) + T^{-}(x), \tag{A16b}$$

where $\iota = h^{\mathrm{s}} k / k^{\mathrm{s}}$ measures the effective thermal insulation of the substrate.

Next we integrate (A10b) and impose (A12) to give the leading-order pressure in the fluid, namely,

$$p = Ap - \frac{\epsilon^3}{\mathrm{Bo}}\frac{\partial^2 h}{\partial x^2} + \epsilon \cot\theta (h - y). \tag{A17}$$

Substituting (A17) into (A10a), we derive an equation governing the horizontal velocity, namely,

$$\frac{\partial^2 v}{\partial y^2} = -1 + A\frac{\partial p}{\partial x} + \epsilon \cot\theta \frac{\partial h}{\partial x} - \frac{\epsilon^3}{\mathrm{Bo}}\frac{\partial^3 h}{\partial x^3} =: \Lambda(x, t). \tag{A18}$$

Integrating (A18) and imposing boundary conditions (A12b) and (A14a) yields

$$v = \frac{y(y - 2h)}{2}\Lambda(x, t) - By\frac{\partial}{\partial x}\big((h + \iota)p + T^{-}\big). \tag{A19}$$

Substituting the horizontal velocity v into the net mass relation (A7), we obtain the thin-film equation, namely,

$$\frac{\partial h}{\partial t} + \frac{\partial}{\partial x}\left[\frac{h^3}{3}\left(1 - A\frac{\partial p}{\partial x} - \alpha\frac{\partial h}{\partial x} + \beta\frac{\partial^3 h}{\partial x^3}\right) - B\frac{h^2}{2}\frac{\partial}{\partial x}\big((h + \iota)p + T^{-}(x)\big)\right] = 0, \tag{A20}$$

where we have defined $\alpha = \epsilon \cot\theta$ and $\beta = \epsilon^3/\mathrm{Bo}$. In the absence of the external (nongravitational) forcing, that is, when $dT^{-}/dx = A = B = 0$, Eq. (A20) admits the steady solution $h \equiv 1$ without loss of generality. Denoting the steady free-surface deflections caused by steady external forcing by $\hbar$, defined by $h(x) = 1 + \hbar(x)$, we find that $\hbar$ is governed by (1) of the main text, where $\hbar$ and its derivatives vanish in the far field, and Q and $\mathcal{T}$ are defined in (2) of the main text. We note that the choice of $\beta = 1$ may always be realized by rescaling the length scale according to the capillary length scale $\mathcal{L}_c := \mathcal{L}\sqrt{\epsilon\gamma/\rho|\boldsymbol{g}|\sin\theta}$.

The study of the steady-state thin-film deflections necessitates some remarks regarding the stability of the full problem. The lubrication approximation we employ neglects inertia at the leading order of the governing equations. Similarly, in the conduction-dominant limit, the temperature is steady to leading order. This ensures that the flow remains a quasisteady function of the film thickness [41]. Therefore the Kapitza instability [39,40], whose onset leads to the development of roll waves [65], is not manifest. To demonstrate this, a linear stability analysis may be performed whereby perturbations to the velocity and temperature fields are quasisteady (with exclusively parametric time dependence through the dependence on the film thickness), since all inhomogeneities are steady and thus time derivatives vanish at all orders. Therefore the stability of the two-dimensional system depends on the validity of the lubrication approximation and the stability of the evolution of the film thickness. To study this we simulate the fully nonlinear transient dynamics of the thin-film equation (A20) using the discretization presented in [66]. Our numerical simulations (not shown here) demonstrate that the steady profiles studied in this work are stable to perturbations for the parameters used in this work. No transient phenomena were observed that would lead to the breakdown of the lubrication approximation (such as steep film gradients, thick regions of film, film dryout, etc.).

The thermocapillary instability introduced in Sec. I is predicted to manifest when an associated Marangoni number, equivalent to the quantity $\epsilon\,\mathrm{Ma}\,/\,\mathrm{Pe}$ in this study, exceeds a critical value (that depends on other system parameters [42]). The critical values predicted theoretically lie approximately in the interval (4,10), with experimentally observed critical values slightly smaller. For the parameters in this study, the quantity $\epsilon\,\mathrm{Ma}\,/\,\mathrm{Pe}$ may be up to two orders of magnitude smaller than this critical value. Nevertheless, the model considered in this study is not identical to those previously investigated. In [41,42] there is no external pressure applied

to the film, and the thermal boundary conditions at the free surface describe Newton's law of cooling, capturing the heat exchange between the ambient gas and the fluid. In this study there is an external pressure source, and we impose a spatially inhomogeneous thermal flux at the free surface, since in the fusion context the fluid is in contact with a vacuum; thus no heat exchange occurs with the surroundings by Newton's law of cooling. A full three-dimensional stability analysis for the model we study is beyond the scope of this work.

Thin-film equations governing the evolution of a free surface, such as (A20), are often referred to as Benney equations, having been first derived by Benney [35]. While some such models prove to exhibit nonphysical features such as finite-time blowup, the fact that inertial effects are negligible and the material properties of interest are taken to be constant in this study suggests that the model will be a good approximation of the physical process [67].

APPENDIX B: NUMERICAL APPROACHES IN OPTIMAL CONTROL

For more comprehensive surveys, we refer the reader to [[68–70], and references therein]. For our purposes it suffices to outline two major directions: indirect and direct numerical approaches. The indirect approach seeks to solve the forward and adjoint equations. This so-called two-point boundary value problem comprises the four ODEs given in Eqs. (8) and (11) and the four boundary conditions of Eqs. (9) and (12). While many classical boundary-problem techniques, such as shooting, may be employed, we implement the forward-backward method [71,72]. An initial guess is made for the control u and boundary condition $\hat{h}(X)$. The dynamics 7b are integrated forward (that is, from $x = -X$ through to $x = X$) numerically to give the first iterate of the state $\hat{h}(x)$. This iterate is then employed in integrating the adjoint problem backwards (that is, from $x = X$ through to $x = -X$) to produce the first iterate of the costate. Using the first iterates of state and costate, we update the control via (17). This procedure is repeated until iterates converge and the boundary conditions are satisfied.

This indirect method is plagued by high sensitivity to the initial guess [68,73], which is particularly challenging for the current problem since its ellipticity renders it ill posed as an initial value problem (IVP). When reinstating normal capillarity [the case of $\beta = \mathcal{O}(1)$], the two-point boundary value problem is formally ill posed due to the infinite switching [50].

These obstacles motivate the second numerical approach, known as the direct approach, whereby the optimal control problem is discretized and solved directly as a nonlinear program (NLP) using generic mathematical programming techniques. This approach dichotomy may be thought of as optimize-then-discretize versus discretize-then-optimize. Each approach has advantages and disadvantages, and which is more suitable depends on features of the problem at hand [68–70].

There are several classes of direct numerical solutions, and we follow [[69], Sec. 8.6] in broadly categorizing them as sequential and simultaneous. In direct sequential solvers, only the control is discretized. The constraining ODE is solved in an inner loop, and the control is updated in an outer loop. This approach (called shooting methods in [68,70], although distinct from the boundary-value shooting mentioned above) is easy to implement but suffers from several drawbacks, including convergence issues [70] due to the highly nonlinear behavior of the constraints with respect to the variables [68]. The reason for this is that small changes at the beginning of the domain may evolve into large deviations as they propagate through the domain. In our setting this problem is exacerbated since the ODE constraint is not well posed as an IVP and thus is highly sensitive to small changes. A common way to remedy this sensitivity is to apply multiple shooting [74], where the domain of integration is split into several intervals, and new decision variables are added as initial conditions on each new interval. Continuity constraints are added so that the solution may be continuously patched together. The result is a higher dimensional NLP (since the initial conditions on each interval are now decision variables), but because each interval is integrated independently, small changes in the initial conditions are propagated only in each interval but not the entire domain. This reduced sensitivity makes the multiple shooting a more robust approach. However, as will be demonstrated when reinstating normal capillarity, we need particularly fine-grained resolution of the control.

Simultaneous solvers are best suited for this purpose, where the full problem is discretized, that is, both the control and the state. We choose a simple finite-difference scheme to discretize the ODE, encoding the discrete formulation using CASADI [75], a framework that performs automatic differentiation to pass gradient information to the IPOPT solver [76], which employs an interior-point method. In this way we leverage the power of state-of-the-art NLP architecture to obtain high resolution in the control. While we found the solution to be largely insensitive to the finite-difference scheme, we found that the smallest stencils yielded the finest control resolution.

APPENDIX C: CHATTERING

In the 1960s Fuller [77] first considered the seemingly simple optimal control problem of minimizing the square displacement of a particle while controlling its acceleration:

$$\min_{|u|\leqslant 1} \frac{1}{2}\int_0^\infty x_1(t)^2 dt, \tag{C1a}$$

subject to

$$\frac{dx_1}{dt} = x_2, \quad \frac{dx_2}{dt} = u, \tag{C1b-c}$$

along with some nontrivial initial condition. Incredibly, it turns out that the bang-bang control that solves (C1) switches infinitely many times in a finite interval before arriving at the origin. This control behavior is called Fuller's phenomenon or chattering (or sometimes Zeno behavior in reference to Zeno and his paradox [17], see also [78–81] for discussions about related but distinct notions of chattering). Chattering was for a long time considered anomalous until the seminal work by Kupka [82] proved that for sufficiently high-order systems chattering is ubiquitous (see [83] for a more extensive treatment and extension of Kupka's results).

A junction is a point at which nonsingular and singular arcs meet. The junctions in Fig. 3(a) are located relatively far from the origin, $|x| \approx 5$, and since $p(x) = e^{-x^2}$, the external forcing near these points is exceedingly small. Similarly, since $\hbar$ is continuous and identically zero on the singular arc, we may assume that $\hbar$ and its derivatives are vanishingly small near the junctions. When these terms are neglected, f defined in (19e) admits the approximation

$$f \approx \frac{B\mathcal{T}(0)}{\beta Q(0)}\, u. \tag{C2}$$

From (19), (22), (24), and (C2) we deduce that, local to the junction in the nonsingular region, assuming that derivatives $d^i\phi/dx^i$ are negligible for $i = 0, \ldots, 5$, the switching function is approximated by the solution of the nonlinear ODE

$$\frac{d^6\phi}{dx^6} \approx U\left(\frac{B\mathcal{T}(0)}{\beta Q(0)}\right)^2 \operatorname{sgn}\phi. \tag{C3}$$

Equation (C3) is homogeneous with respect to x, and therefore solutions are translation invariant and we consider the junction to be located at the origin $x = 0$ without loss of generality. To further simplify the presentation, we scale x with the inverse of the sixth root of the coefficient $U[B\mathcal{T}(0)/\beta Q(0)]^2$ to obtain the scaled approximation

$$\frac{d^6\phi}{dx^6} = \operatorname{sgn}\phi. \tag{C4}$$

Adapting the analysis of Fuller's original problem in [78], we note that the switching equation (C4) is invariant under the transform $\phi(x) \mapsto J^6\phi(x/J)$. We leverage this symmetry to uncover the structure of the switching by seeking a self-similar solution of (C4). Our aim is to construct a smooth solution of (C4) on an interval where ϕ is of one sign, vanishing at the endpoints. We then extend this solution self-similarly to an adjacent interval. Enforcing sufficient smoothness will allow us to determine valid values of J and thus determine ϕ. Note that the form of the symmetry validates the earlier assumption of vanishingly small derivatives up to fifth order near the junction.

We assume that a solution ϕ has adjacent zeros at x_0 and x_1 where $x_0 < x_1 < 0$ and is positive in the intervening interval. Integrating (C4) we find that, on $[x_0, x_1]$, ϕ takes the form

$$\phi(x) = \varphi(x) := \frac{x^6}{6!} + \sum_{i=0}^{5} c_i x^i, \quad \text{for} \quad x \in [x_0, x_1]. \tag{C5}$$

We use the symmetry parameter J to construct a self-similar copy on the adjacent segment defined by $[x_1, x_2] = [x_0 J, x_1 J]$. In defining the adjacent segment with $x_0 J = x_1 > x_0$, we implicitly require that $0 < J < 1$ (since x_i are negative, and we neglect $J < 0$ since the adjacent segment must remain on the same side of the junction which is taken to be the origin). This assumption is without loss of generality, as $J > 1$ could equally be considered, with the adjacent segment being $[x_{-1}, x_0] = [x_0 J, x_1 J]$. The former construction has adjacent segments of decreasing length converging to the origin, while the latter has adjacent segments of increasing length diverging from the origin. Thus the construction with J and the adjacent interval to the right is equivalent to that with $1/J$ and the interval to the left.

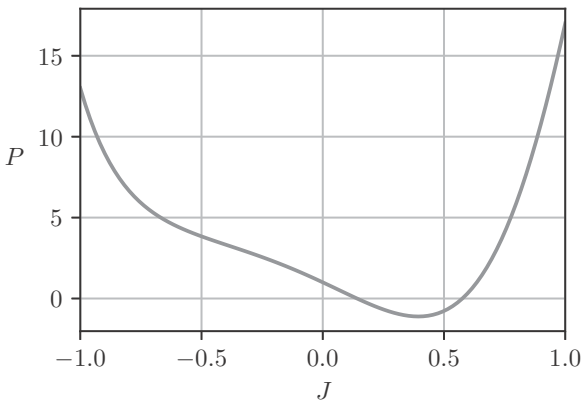

FIG. 8. Polynomial $P(J)$ defined in (C8).

On the adjacent segment, the solution is given by

$$\phi(x) = -J^6\varphi(x/J), \quad \text{for} \quad x \in [x_1, x_2]. \tag{C6}$$

Requiring continuity of derivatives up to fifth order at the shared boundary point $x = x_1$ yields six constraints:

$$\lim_{x\uparrow x_1} \frac{d^i\phi}{dx^i}(x) = \lim_{x\downarrow x_1} \frac{d^i\phi}{dx^i}(x), \quad \text{for} \quad i = 0, \ldots, 5, \tag{C7}$$

which suffice to determine the six unknowns c_i. Finally, enforcing the zero $\phi(x_1) = 0$, we find that J is a root of the polynomial P given by

$$P(J) = J^8 - 7J^7 - 2J^6 + 8J^5 + 17J^4 + 8J^3 - 2J^2 - 7J + 1. \tag{C8}$$

It follows from the symmetry of the coefficients of P that $P(J) = 0$ if and only if $P(1/J) = 0$, reflecting the aforementioned equivalence. Therefore all roots of P are characterized by roots in the interval $J \in [-1, 1]$, and we see by plotting $P(J)$ in Fig. 8 that there are two: $J \approx 0.141\,408$ and $J \approx 0.575\,736$.

It is worthwhile to briefly take stock of what we have achieved. We have neglected exceedingly small terms to obtain an equation (C4) approximately governing the switching function ϕ. We then utilized an invariance of (C4) to construct self-similar solutions. The zeros of these solutions form a geometric sequence with ratio J, given by a root of the polynomial (C8), and thereby give rise to a "fractal" optimal control. As discussed at the end of Sec. IV, the analytical switching points predicted by this solution structure agrees remarkably well with the numerical solution [see Fig. 3(b)].

Notably, the first-order system and its adjoint (8), (9), (11) and (12) admit an analogous approximate switching equation when $\alpha > 0$, namely,

$$\frac{d^2\phi}{dx^2} \approx -U\left(\frac{B\mathcal{T}(0)}{\alpha Q(0)}\right)^2 \operatorname{sgn}(\phi). \tag{C9}$$

It is straightforward to show that any nontrivial solution of (C9) is a concatenation of identical parabolic arcs of alternating sign; all roots are uniformly separated, thus no switching can occur (in regions where this approximation is valid).

[1] R. V. Craster and O. K. Matar, Dynamics and stability of thin liquid films, Rev. Mod. Phys. **81**, 1131 (2009).

[2] T. G. Myers, Thin films with high surface tension, SIAM Rev. **40**, 441 (1998).

[3] A. Oron, S. H. Davis, and S. G. Bankoff, Long-scale evolution of thin liquid films, Rev. Mod. Phys. **69**, 931 (1997).

[4] P. Fiflis, M. Christenson, M. Szott, K. Kalathiparambil, and D. N. Ruzic, Free surface stability of liquid metal plasma facing components, Nucl. Fusion **56**, 106020 (2016).

[5] D. Lunz, Dynamics and stability of a thin liquid lithium flow within a tokamak divertor, D.Phil., University of Oxford, 2019.

[6] M. Ono, R. Majeski, M. A. Jaworski, Y. Hirooka, R. Kaita, T. K. Gray, R. Maingi, C. H. Skinner, M. Christenson, and D. N. Ruzic, Liquid lithium loop system to solve challenging technology issues for fusion power plant, Nucl. Fusion **57**, 116056 (2017).

[7] P. D. Fowler, C. Ruscher, J. D. McGraw, J. A. Forrest, and K. Dalnoki-Veress, Controlling Marangoni-induced instabilities in spin-cast polymer films: How to prepare uniform films, Eur. Phys. J. E **39**, 90 (2016).

[8] J. J. Kriegsmann, M. J. Miksis, and J.-M. Vanden Broeck, Pressure driven disturbances on a thin viscous film, Phys. Fluids **10**, 1249 (1998).

[9] J. Quintans Carou, S. K. Wilson, N. J. Mottram, and B. R. Duffy, Asymptotic and numerical analysis of a simple model for blade coating, J. Eng. Math. **63**, 155 (2008).

[10] E. O. Tuck and J.-M. Vanden Broeck, Influence of surface tension on jet-stripped continuous coating of sheet materials, AIChE J. **30**, 808 (1984).

[11] R. P. Haskett, T. P. Witelski, and J. Sur, Localized Marangoni forcing in driven thin films, Physica D **209**, 117 (2005).

[12] B. Scheid, A. Oron, P. Colinet, U. Thiele, and J. C. Legros, Nonlinear evolution of nonuniformly heated falling liquid films, Phys. Fluids **14**, 4130 (2002).

[13] D. P. Frisk and E. J. Davis, The enhancement of heat transfer by waves in stratified gas–liquid flow, Int. J. Heat Mass Transfer **15**, 1537 (1972).

[14] A. Miyara, Numerical analysis on flow dynamics and heat transfer of falling liquid films with interfacial waves, Heat Mass Transfer **35**, 298 (1999).

[15] K. Serifi, N. A. Malamataris, and V. Bontozoglou, Transient flow and heat transfer phenomena in inclined wavy films, Int. J. Therm. Sci. **43**, 761 (2004).

[16] H. Kwakernaak and R. Sivan, *Linear Optimal Control Systems* (John Wiley & Sons, Inc., New York, 1972).

[17] D. Liberzon, *Calculus of Variations and Optimal Control Theory: A Concise Introduction* (Princeton University Press, Princeton, NJ, 2011).

[18] A. K. Nagy and R. D. Braatz, Open-loop and closed-loop robust optimal control of batch processes using distributional and worst-case analysis, J. Process Control **14**, 411 (2004).

[19] N. Garnier, R. O. Grigoriev, and M. F. Schatz, Optical Manipulation of Microscale Fluid Flow, Phys. Rev. Lett. **91**, 054501 (2003).

[20] R. O. Grigoriev, Control of evaporatively driven instabilities of thin liquid films, Phys. Fluids **14**, 1895 (2002).

[21] A. C. Or, R. E. Kelly, L. Cortelezzi, and J. L. Speyer, Control of long-wavelength Marangoni–Bénard convection, J. Fluid Mech. **387**, 321 (1999).

[22] J. Tang and H. H. Bau, Stabilization of the No-Motion State in Rayleigh–Bénard Convection through the Use of Feedback Control, Phys. Rev. Lett. **70**, 1795 (1993).

[23] M. G. Blyth and A. P. Bassom, Flow of a liquid layer over heated topography, Proc. R. Soc. London, Ser. A **468**, 4067 (2012).

[24] M. Amaouche, H. A. Abderrahmane, and L. Bourdache, Hydromagnetic thin film flow: Linear stability, Phys. Rev. E **88**, 023028 (2013).

[25] D. Tseluiko, M. G. Blyth, D. T. Papageorgiou, and J.-M. Vanden-Broeck, Effect of an electric field on film flow down a corrugated wall at zero Reynolds number, Phys. Fluids **20**, 042103 (2008).

[26] D. Tseluiko, M. G. Blyth, D. T. Papageorgiou, and J.-M. Vanden-Broeck, Electrified viscous thin film flow over topography, J. Fluid Mech. **597**, 449 (2008).

[27] D. Tseluiko and D. T. Papageorgiou, Wave evolution on electrified falling films, J. Fluid Mech. **556**, 361 (2006).

[28] S. Veremieiev, H. Thompson, M. Scholle, Y. Lee, and P. Gaskell, Electrified thin film flow at finite Reynolds number on planar substrates featuring topography, Int. J. Multiphase Flow **44**, 48 (2012).

[29] B. Park and Y. Cho, Experimental observation of gravity–capillary solitary waves generated by a moving air suction, J. Fluid Mech. **808**, 168 (2016).

[30] A. B. Thompson, D. Tseluiko, and D. T. Papageorgiou, Falling liquid films with blowing and suction, J. Fluid Mech. **787**, 292 (2015).

[31] A. Armaou and P. D. Christofides, Feedback control of the Kuramoto–Sivashinsky equation, Physica D **137**, 49 (2000).

[32] A. Armaou and P. D. Christofides, Wave suppression by nonlinear finite-dimensional control, Chem. Eng. Sci. **55**, 2627 (2000).

[33] Y. Lou and P. D. Christofides, Optimal actuator/sensor placement for nonlinear control of the Kuramoto–Sivashinsky equation, IEEE Trans. Control Syst. Technol. **11**, 737 (2003).

[34] A. B. Thompson, S. N. Gomes, G. A. Pavliotis, and D. T. Papageorgiou, Stabilising falling liquid film flows using feedback control, Phys. Fluids **28**, 012107 (2016).

[35] D. J. Benney, Long waves in liquid films, J. Math. Phys. **45**, 150 (1966).

[36] B. Gjevik, Occurrence of finite-amplitude surface waves on falling liquid films, Phys. Fluids **13**, 1918 (1970).

[37] T. Eich, B. Sieglin, A. Scarabosio, W. Fundamenski, R. J. Goldston, and A. Herrmann, Inter-ELM Power Decay Length for JET and ASDEX Upgrade: Measurement and Comparison with Heuristic Drift-Based Model, Phys. Rev. Lett. **107**, 215001 (2011).

[38] D. Lunz and P. D. Howell, Dynamics of a thin film driven by a moving pressure source, Phys. Rev. Fluids **3**, 114801 (2018).

[39] P. L. Kapitza, Wave flow of thin layer of viscous fluid, Zh. Eksp. Teor. Fiz. **18**, 3 (1948).

[40] C.-S. Yih, Stability of liquid flow down an inclined plane, Phys. Fluids **6**, 321 (1963).

[41] S. Kalliadasis, A. Kiyashko, and E. A. Demekhin, Marangoni instability of a thin liquid film heated from below by a local heat source, J. Fluid Mech. **475**, 377 (2003).

[42] J. M. Skotheim, U. Thiele, and B. Scheid, On the instability of a falling film due to localized heating, J. Fluid Mech. **475**, 1 (2003).

[43] D. Léonard and N. Long, *Optimal Control Theory and Static Optimization in Economics* (Cambridge University Press, Cambridge, United Kingdom, 1992).
[44] A. L. Bertozzi, A. Münch, and M. Shearer, Undercompressive shocks in thin film flows, Physica D **134**, 431 (1999).
[45] R. Hartl, S. Sethi, and R. Vickson, A survey of the maximum principles for optimal control problems with state constraints, SIAM Rev. **37**, 181 (1995).
[46] L. S. Pontryagin, V. G. Boltyanskii, R. V. Gamkrelidze, and E. F. Mishchenko, *The Mathematical Theory of Optimal Processes* (John Wiley & Sons, New York, 1962).
[47] R. Lewis, Definitions of order and junction conditions in singular optimal control problems, SIAM J. Control Optim. **18**, 21 (1980).
[48] J. McDanell and W. F. Powers, Necessary conditions joining optimal singular and nonsingular subarcs, SIAM J. Control Optim. **9**, 161 (1971).
[49] H. M. Robbins, A generalized Legendre–Clebsch condition for the singular cases of optimal control, IBM J. Res. Dev. **11**, 361 (1967).
[50] M. Caponigro, R. Ghezzi, B. Piccoli, and E. Trélat, Regularization of chattering phenomena via bounded variation controls, IEEE Trans. Autom. Control **63**, 2046 (2018).
[51] A. Levant, Higher-order sliding modes, differentiation and output-feedback control, Int. J. Control **76**, 924 (2003).
[52] L. G. Leal, *Advanced Transport Phenomena*, *Cambridge Series in Chemical Engineering* (Cambridge University Press, Cambridge, England, 2007).
[53] N. B. Morley, A. A. Gaizer, and M. A. Abdou, Estimates of the effect of a plasma momentum flux on the free surface of a thin film of liquid metal, Fusion Eng. Des. **28**, 176 (1995).
[54] U. Samm, Plasma-wall interaction in magnetically confined fusion plasmas, Fusion Sci. Technol. **57**, 241 (2010).
[55] L. J. Haworth and L. D. P. King, The stopping power of lithium for low energy protons, Phys. Rev. **54**, 48 (1938).
[56] C. Liao, M. S. Kazimi, and B. LaBombard, MHD effects on liquid metal film flow, Nucl. Eng. Des. **146**, 325 (1994).
[57] J. Blumm, A. Lindemann, B. Niedrig, and R. Campbell, Measurement of selected thermophysical properties of the NPL certified reference material stainless steel 310, Int. J. Thermophys. **28**, 674 (2007).
[58] H. W. Davison, Compilation of thermophysical properties of liquid lithium, Tech. Rep. Lewis Research Center, NASA, Cleveland, OH, 1968 (unpublished).
[59] D. Lunz and P. D. Howell, Flow of a thin liquid-metal film in a toroidal magnetic field, J. Fluid Mech. **867**, 835 (2019).
[60] E. Platacis, A. Flerov, A. Klukin, S. Ivanov, A. Sobolevs, A. Shishko, L. Zaharov, and M. Gryaznevich, Gravitational flow of a thin film of liquid metal in a strong magnetic field, Fusion Eng. Des. **89**, 2937 (2014).
[61] M. A. Jaworski, S. P. Gerhardt, N. B. Morley, T. Abrams, R. Kaita, J. Kallman, H. Kugel, R. Majeski, and D. N. Ruzic, Macroscopic motion of liquid metal plasma facing components in a diverted plasma, J. Nucl. Mater. **415**, S985 (2011).
[62] M. A. Jaworski, T. K. Gray, M. Antonelli, J. J. Kim, C. Y. Lau, M. B. Lee, M. J. Neumann, W. Xu, and D. N. Ruzic, Thermoelectric Magnetohydrodynamic Stirring of Liquid Metals, Phys. Rev. Lett. **104**, 094503 (2010).
[63] D. N. Ruzic, W. Xu, D. Andruczyk, and M. A. Jaworski, Lithium–metal infused trenches (LiMIT) for heat removal in fusion devices, Nucl. Fusion **51**, 102002 (2011).
[64] W. Xu, D. Curreli, D. Andruczyk, T. Mui, R. Switts, and D. N. Ruzic, Heat transfer of TEMHD driven lithium flow in stainless steel trenches, J. Nucl. Mater. **438**, S422 (2013).
[65] N. J. Balmforth and S. Mandre, Dynamics of roll waves, J. Fluid Mech. **514**, 1 (2004).
[66] L. Zhornitskaya and A. L. Bertozzi, Positivity-preserving numerical schemes for lubrication-type equations, SIAM J. Numer. Anal. **37**, 523 (1999).
[67] B. Scheid, C. Ruyer-Quil, U. Thiele, O. A. Kabov, J. C. Legros, and P. Colinet, Validity domain of the Benney equation including the Marangoni effect for closed and open flows, J. Fluid Mech. **527**, 303 (2005).
[68] J. T. Betts, Survey of numerical methods for trajectory optimization, J. Guid. Control Dyn. **21**, 193 (1998).
[69] L. T. Biegler, *Nonlinear Programming: Concepts, Algorithms, and Applications to Chemical Processes* (SIAM, Philadelphia, PA, 2010).
[70] E. Trélat, Optimal control and applications to aerospace: Some results and challenges, J. Optim. Theory Appl. **154**, 713 (2012).
[71] F. L. Chernousko and A. A. Lyubushin, Method of successive approximations for solution of optimal control problems, Optim. Control Appl. Methods **3**, 101 (1982).
[72] M. McAsey, L. Mou, and W. Han, Convergence of the forward-backward sweep method in optimal control, Comput. Optim. Appl. **53**, 207 (2012).
[73] J. Zhu, E. Trélat, and M. Cerf, Geometric optimal control and applications to aerospace, Pacific J. Math. Ind. **9**, 8 (2017).
[74] H. G. Bock and K. J. Plitt, A multiple shooting algorithm for direct solution of optimal control problems, IFAC Proc. **17**, 1603 (1984).
[75] J. A. E. Andersson, J. Gillis, G. Horn, J. B. Rawlings, and M. Diehl, CasADi: A software framework for nonlinear optimization and optimal control, Math. Program. Comput. **11**, 1 (2019).
[76] A. Wächter and L. T. Biegler, On the implementation of an interior-point filter line-search algorithm for large-scale nonlinear programming, Math. Program. **106**, 25 (2006).
[77] A. T. Fuller, Study of an optimum non-linear control system, J. Electron. Control **15**, 63 (1963).
[78] C. Marchal, Chattering arcs and chattering controls, J. Optim. Theory Appl. **11**, 441 (1973).
[79] L. Fridman and A. Levant, Higher order sliding modes as a natural phenomenon in control theory, in *Robust Control via Variable Structure and Lyapunov Techniques*, edited by F. Garofalo and L. Glielmo (Springer, Berlin, Heidelberg, 1996), pp. 107–133.
[80] G. Bartolini, A. Ferrara, and E. Usai, Chattering avoidance by second-order sliding mode control, IEEE Trans. Autom. Control **43**, 241 (1998).
[81] V. Utkin and H. Lee, Chattering problem in sliding mode control systems, IFAC Proc. **39**, 1 (2006).
[82] I. A. K. Kupka, The ubiquity of Fuller's phenomenon, in *Nonlinear Controllability and Optimal Control*, edited by H. J. Sussman (CRC Press, Boca Raton, FL, 1990), Chap. 11, pp. 313–350.
[83] M. I. Zelikin and V. F. Borisov, *Theory of Chattering Control: With Applications to Astronautics, Robotics, Economics, and Engineering* (Birkhäuser, Boston, 1994).